75th International Astronautical Congress (IAC), Milan, Italy, 14-18 October 2024.
Copyright © 2024 by the authors. Published by the IAF, with permission and released to the IAF to publish in all forms.

IAC–24–C1.8.6

Bridging Ephemeris Transition Gaps: Quasi-Periodic Extensions for the Hill Restricted Four-Body Problem in Cislunar Space

Beom Park[a]*, **Rohith Reddy Sanaga**[b], **Kathleen C. Howell**[c]

[a] *PhD Candidate, School of Aeronautics and Astronautics, Purdue University, U.S.*, park1103@purdue.edu
[b] *PhD Candidate, School of Aeronautics and Astronautics, Purdue University, U.S.*, rsanaga@purdue.edu
[c] *Hsu Lo Distinguished Professor of Aeronautics and Astronautics, School of Aeronautics and Astronautics, Purdue University, U.S.*, howell@purdue.edu
* Corresponding Author

Abstract

In the cislunar environment, the Earth-Moon Circular Restricted Three-Body Problem (CR3BP) is widely recognized as a valuable dynamical model, providing essential structures for the preliminary design process. However, for these trajectories to be practically applicable in flight, validation in a Higher-Fidelity Ephemeris Model (HFEM) is imperative. For this transition process, more insights are gained via employing intermediate dynamical models that enable numerical continuation and bifurcation analysis within the context of Hamiltonian structures. In particular, quasi-periodic extensions to the Hill Restricted Four-Body Problem (HR4BP) are proposed in recent literature that allow (i) coherent representation of solar gravity and (ii) incorporation of two incommensurate perturbing frequencies in addition to the CR3BP dynamics, serving as suitable "next steps" in bridging the gap between the CR3BP and HFEM. The current analysis extends these Quasi-Hill Restricted Four-Body Problems (QHR4BPs), elucidating different aspects in numerical implementation. The models are comprised of two components: (i) describing the Earth-Moon motion under solar gravity within the Hill Three-Body Problem (H3BP) and (ii) representing the spacecraft dynamics under the influence from the Sun-Earth-Moon system. Several alternatives for these components are explored, highlighting the general trade-offs between implementation complexity and their effectiveness as medium-fidelity models in the transition from lower- to higher-fidelity frameworks. Lastly, the model is further enhanced to incorporate three incommensurate frequencies by utilizing three-dimensional quasi-periodic orbits for representing the Earth-Moon motion. The capability of the model is demonstrated for the Earth-Moon L_2 9:2 synodic resonant halo orbit, where the quasi-periodic extensions for the HR4BP provide further insights into the complex behavior as observed in the HFEM.
Keywords: CR3BP, HR4BP, Cislunar space, Ephemeris transition, Model hierarchy

1. Introduction

While the dynamical environment within the cislunar domain is undoubtedly complex, idealized Hamiltonian systems offer significant insight in describing the evolution of motion for artificial objects. The Earth-Moon Circular Restricted Three-Body Problem (CR3BP) often serves as a suitable lower-fidelity dynamical model that incorporates both the Earth and Moon; it supplies an autonomous model within a rotating frame. Based on the theoretical foundation provided in Gómez, Masdemont, and Mondelo [1], then, a Sun-Earth-Moon point-mass HFEM is approximated as multi-dimensional quasi-periodic dynamical model within a common rotating frame. Via this insight, a frequency-based model hierarchy is envisioned in the cislunar regime in Park, Sanaga, and Howell [2], where various time-dependent Hamiltonian systems are understood as bridging the gap between the autonomous CR3BP and multi-dimensional frequency HFEM, characterized by the number of perturbing frequencies incorporated in addition to the CR3BP. For periodically perturbed models, one frequency is added to the CR3BP, e.g., the Elliptic Restricted Three-Body Problem (ER3BP) and the Hill Restricted Four-Body Problem (HR4BP). Park, Sanaga, and Howell [2] also propose quasi-periodically perturbed models that add two incommensurate frequencies to the CR3BP that extend the HR4BP [3]. These quasi-periodic models serve as suitable "next steps" within the model hierarchy while maintaining the coherent solar gravity property [2, 4].

The main objective of the current analysis is enhancing the quasi-periodic extensions for the HR4BP within the context of the model hierarchy in the cislunar domain, focusing on two aspects. Firstly, numerical implementation for the QHR4BPs is detailed, addressing multiple options in formulating the dynamics. The previously proposed QHR4BPs leverage two-dimensional (2D) Quasi-Periodic Orbits (QPOs) to represent the Earth-Moon gravitational motion, where a set of assumptions facilitate im-

Copyright © 2024 by the authors. Published by the IAF, with permission and released to the IAF to publish in all forms.

plementations with varying complexities and accuracies. Then, the spacecraft is described under the influence of the Sun-Earth-Moon gravitational system, where two notable options arise for rotating reference frames. Capabilities of these frames in drawing various insights as well as a proper frame rotation scheme are detailed in the current analysis. Secondly, the QHR4BP is further extended to leverage a three-dimensional (3D) QPO representation for the Earth-Moon motion. This extension allows incorporation of three incommensurate frequencies in addition to the CR3BP, further bridging the model hierarchy between the CR3BP and HFEM in the cislunar domain.

2. Frames and Independent Variables

Frames and independent variables are briefly reviewed, following the analysis in Park, Sanaga, and Howell [2]. The letters S, E, M, B, c denote the Sun, Earth, Moon, Earth-Moon barycenter, and spacecraft, respectively. The Hill frame (Fig. 1(a)) is leveraged to represent the H3BP dynamics, adopting a Sun-B (Earth-Moon Barycenter) rotating frame centered at B. The nondimensional (nd) vector $\vec{r}_{EM}$ denotes the lunar position with respect to the Earth, nondimensionalized by $l_H = l_{SB*}((\tilde{\mu}_E + \tilde{\mu}_M)/\tilde{\mu}_S)^{1/3}$ with the dimensional standard gravitational parameter $\tilde{\mu}$ for each body, e.g., $\tilde{\mu}_E \approx 398600\ \mathrm{km}^3/\mathrm{s}^2$. The constant Sun-$B$ distance is denoted as l_{SB*}. The orthonormal unit vectors for the frame are $\hat{i}_H - \hat{j}_H - \hat{k}_H$. Thus, the Earth-Moon nd position vector is expressed as,

$$\vec{r}_{EM} = \xi \hat{i}_H + \eta \hat{j}_H + \zeta \hat{k}_H, \tag{1}$$

in the Hill frame. The out-of-plane direction $\hat{k}_H$ is inertially fixed, and the in-plane unit vectors are rotating at a constant rate with respect to $\hat{k}_H$. The second frame, uniform-rotating frame (Fig. 1(b)), represents a Earth-Moon rotating frame to describe the nd spacecraft position vector, $\vec{\rho}_*$, with respect to the origin at B. A constant length l_* is leveraged to nondimensionalize length within the frame, tracking the average Earth-Moon distance. The unit vectors for the frame are $\hat{x}_* - \hat{y}_* - \hat{z}_*$. Note that $\hat{z}_* = \hat{k}_H$ and, thus, it is inertially fixed. The in-plane vectors $\hat{x}_* - \hat{y}_*$ rotate at a constant rate with respect to $\hat{z}_*$. For a general Earth-Moon motion, the Earth and Moon are not stationary in the uniform-rotating frame as depicted by grey round arrows in Fig. 1(b). The third frame, the pulsating-rotating frame (Fig. 1(c)), adopts stationary locations for the Earth and the Moon, describing the spacecraft position vector as $\vec{\rho}$. The unit vectors for the frame are defined as: (i) $\hat{x}$ is directed from the Earth to the Moon, (ii) $\hat{z}$ coincides with the instantaneous angular momentum vector for the Moon orbit with respect to the Earth, and (iii) $\hat{y}$ is constructed instantaneously to complete the dextral triad. The Earth and Moon locations are fixed at $-\mu$ and $(1-\mu)$ on the $\hat{x}$-axis for $\mu = \tilde{\mu}_M/(\tilde{\mu}_E + \tilde{\mu}_M)$. Thus, the spacecraft nd position vector within the frame is rendered as,

$$\vec{\rho} = x\hat{x} + y\hat{y} + z\hat{z}. \tag{2}$$

The three different frames are adopted to yield various insights for the QHR4BPs.

Three nd time variables are relevant for the current analysis, corresponding to: τ, the Hill time, τ_3, the H3BP time, and t, the pulsating nd time. For the dimensional time variable, T, $d\tau/dT = \tau' = 1/m\sqrt{\tilde{\mu}_S/l_{SB*}^3}$ for $m \approx 0.0808$ defined such that $(1+m)$ tracks the ratio of the synodic lunar month to the sidereal lunar month. Then, $\tau_3 = m\tau$; thus, τ, τ_3, and T are uniformly scaled to each other. The last nd variable is constructed in a non-uniform fashion, i.e., $dt/dT = \sqrt{(\tilde{\mu}_E + \tilde{\mu}_M)/l^3}$ for an instantaneously evaluated dimensional Earth-Moon distance, $l = l(T)$. While it is possible to describe the evolution of vectors in a reference frame with respect to *any* time variables, certain combinations yield additional insights.

The Hill frame and the uniform-rotating frame (Figs. 1(a) and 1(b)) rotate with respect to the common out-of-plane direction $\hat{k}_H = \hat{z}_*$ that is inertially fixed. The constant angular rates are: unity for the Hill frame, measured in τ_3, and $(1+m)$ for the uniform-rotating frame, measured in τ. Thus, the direction cosine matrix between these two frames are evaluated as,

$$\boldsymbol{C}_H^* = \begin{bmatrix} \cos\tau & \sin\tau & 0 \\ -\sin\tau & \cos\tau & 0 \\ 0 & 0 & 1 \end{bmatrix}, \tag{3}$$

assuming that $\hat{i}_H = \hat{x}_*$ at the initial epoch. From Eqs. (1) and (3), the Earth-Moon nd position vector in the uniform-rotating frame is,

$$\vec{\rho}_{EM*} = \frac{l_H \boldsymbol{C}_H^* \vec{r}_{EM}}{l_*} = x_{EM*}\hat{x}_* + y_{EM*}\hat{y}_* + z_{EM*}\hat{z}_*. \tag{4}$$

Rotations involving the pulsating-rotating frame are further examined in subsequent sections.

3. General HR4BP Framework: Two Components

A general Hill Restricted Four-Body Problem (HR4BP) framework is originally introduced in Scheeres [3]. The formulation is characterized by two parallel dynamics components as depicted in Fig. 2. The first component corresponds to the Hill Three-Body Problem (H3BP) dynamics that describe the Earth-Moon configuration under a coherent solar gravity modeling. The solution for this three-body system is then leveraged

Copyright © 2024 by the authors. Published by the IAF, with permission and released to the IAF to publish in all forms.

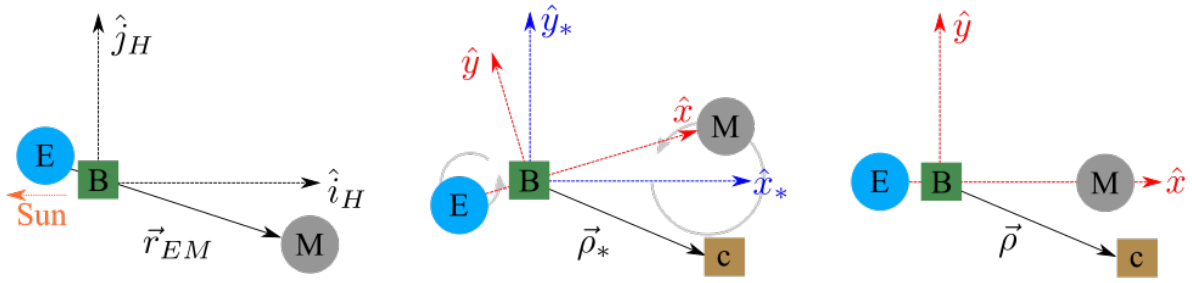

(a) Hill frame (b) Uniform-rotating frame (c) Pulsating-rotating frame

Fig. 1. Frames from Park, Sanaga, and Howell [2]

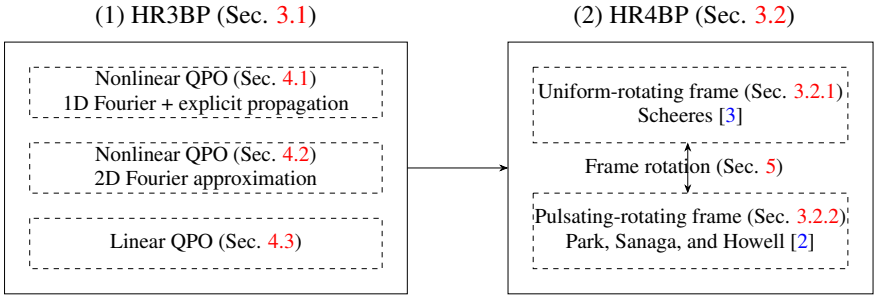

Fig. 2. General HR4BP framework: two parallel components

within the second, HR4BP component, where the equations of motion for the spacecraft are supplied in the restricted four-body model. By a common assumption, the celestial bodies are modeled as point-masses. The Sun-B, or the Earth-Moon barycenter, describes a circular orbit.* Then, any particular solution from the H3BP may be leveraged to represent the Sun-Earth-Moon configuration within the general HR4BP framework. In its original formulation from Scheeres [3], the Lunar Variational periodic Orbit (LVO) is leveraged, facilitating a periodically forced dynamical model as cast within the uniform-rotating frame. The Quasi-periodic extension of the HR4BP requires a quasi-periodic solution for the Sun-Earth-Moon system. For a successful implementation, consideration of multiple options for the two parallel components, i.e., the HR3BP and HR4BP as illustrated in Fig. 2, is imperative.

3.1 H3BP

The Sun-Earth-Moon configuration is approximated as any particular solution in the H3BP dynamics. For the Earth-Moon nd position vector in the Hill frame, i.e., $\vec{r}_{EM} = \xi \hat{i}_H + \eta \hat{j}_H + \zeta \hat{k}_H$, the equations of motion are supplied as,

$$\begin{aligned} \frac{d^2\xi}{d\tau_3^2} &= 2\frac{d\eta}{d\tau_3} + 3\xi - \frac{1}{r_{EM}^3}\xi \\ \frac{d^2\eta}{d\tau_3^2} &= -2\frac{d\xi}{d\tau_3} - \frac{1}{r_{EM}^3}\eta \\ \frac{d^2\zeta}{d\tau_3^2} &= -\zeta - \frac{1}{r_{EM}^3}\zeta. \end{aligned} \tag{5}$$

One particular periodic solution that is associated with a $2m\pi$ period as measured in τ_3 with $m \approx 0.0808$, is the Lunar Variational periodic Orbit (LVO). Thus, the orbit contains the information for the synodic lunar month, and serves as a basis for the Hill and Brown lunar theory [5]. An initial state on the LVO is provided in Table 2 in Appendix. The monodromy matrix for the LVO admits in-plane and out-of-plane center subspaces generally corresponding to, the eccentricity of the Earth-Moon motion, ε, and the inclination of the lunar motion with respect to the Earth ecliptic plane, $\imath$. Two separate families of nonlinear 2D-QPO exist that are tangent to each linear center subspace within the H3BP as demonstrated in Park, Sanaga, and Howell [2]. These families are one-parameter families with orbits of a fixed period that track the synodic lunar month. These QPOs serve as refined approximations for the realistic Earth-Moon motion. For

*While it is possible to describe the Sun-B in terms of an elliptic orbit within the HR4BP [3], it introduces an additional frequency that is generally associated with smaller perturbations within the HFEM that may be considered secondary to other types of perturbations. Refer to Gómez, Masdemont, and Mondelo [1] for this observation.

Copyright © 2024 by the authors. Published by the IAF, with permission and released to the IAF to publish in all forms.

example, consider Fig. 3(a), where the lunar motion from ephemerides is depicted over 20 years in the Hill frame. The LVO corresponds to a one-frequency reduction (periodic approximation) for the lunar ephemerides in the same frame. Then, the in-plane and out-of-plane 2D-QPOs as illustrated in Figs. 3(b) and 3(c) correspond to two-frequency approximations that incorporate the desired ε and ι in addition to the LVO, respectively. Leveraging these 2D-QPOs, the HR4BP is extended to quasi-periodically forced models; various options for approximating the 2D-QPOs are considered within the context of QHR4BPs in Sec. 4.

3.2 HR4BP

Leveraging the solutions from the H3BP, the dynamics for the spacecraft are formulated within the restricted four-body problem. For illustrating the cislunar dynamical environment, it is beneficial to consider Earth-Moon rotating frames. Two options that leverage the uniform-rotating frame and the pulsating-rotating frame are reviewed.

3.2.1 Uniform-rotating frame formulation

The original derivation of the HR4BP from Scheeres [3] leverages the uniform-rotating frame (Fig. 1(b)). Recall that the nd spacecraft position vector in the frame is represented as $\vec{\rho}_* = x_*\hat{x}_* + y_*\hat{y}_* + z_*\hat{z}_*$. Then, within the HR4BP, following acceleration components are supplied,

$$\begin{aligned} \mathring{\mathring{x}}_* &= 2(1+m)\mathring{y}_* + \frac{\partial V}{\partial x_*} \\ \mathring{y}_* &= -2(1+m)\mathring{x}_* + \frac{\partial V}{\partial y_*} \\ \mathring{\mathring{z}}_* &= \frac{\partial V}{\partial z_*}, \end{aligned} \tag{6}$$

where $\mathring{\mathring{x}}_* = d^2x_*/d\tau^2$ and $\mathring{x}_* = dx_*/d\tau$. The pseudo-potential function $V = V(x_*, y_*, z_*, \tau; \mu, m)$ is defined as,

$$\begin{aligned} V = &\frac{1}{2}\left(1 + 2m + \frac{3}{2}m^2\right)(x_*^2 + y_*^2) - \frac{1}{2}m^2 z_*^2 \\ &+ \frac{3}{4}m^2((x_*^2 - y_*^2)\cos 2\tau - 2x_* y_* \sin 2\tau) \\ &+ \frac{m^2}{a_0^3}\left[\frac{1-\mu}{\rho_{Ec*}} + \frac{\mu}{\rho_{Mc*}}\right]. \end{aligned} \tag{7}$$

The quantities ρ_{Ec*} and ρ_{Mc*} are distances from the spacecraft to the Earth and Moon within the uniform-rotating frame, respectively, rendering,

$$\rho_{Ec*} = |\vec{\rho}_* + \mu\vec{\rho}_{EM*}|, \quad \rho_{Mc*} = |\vec{\rho}_* - (1-\mu)\vec{\rho}_{EM*}|, \tag{8}$$

where $\vec{\rho}_{EM*}$ is supplied from the H3BP solution and rotation via Eq. (4). The parameter m connects the Earth-Moon CR3BP ($m = 0$) and the Sun-Earth-Moon system at $m \approx 0.0808$, providing a useful continuation strategy. In the current analysis, m is fixed as $m \approx 0.0808$. Adopting a uniformly rotating frame results in a rather simple form of equations of motion through Eq. (7), where varying the H3BP solution only manifests in evaluating $\vec{\rho}_{EM*}$.

3.2.2 Pulsating-rotating frame formulation

In Park, Sanaga, and Howell [2], the HR4BP dynamics are recast within the pulsating-rotating frame (Fig. 1(c)). Such a formulation is adaptable to multiple independent variables and facilitates comparison with other dynamical models that are often developed within the pulsating-rotating frame. For the nd spacecraft position vector $\vec{\rho} = x\hat{x} + y\hat{y} + z\hat{z}$, the equations of motion are reformulated as follows,

$$\begin{aligned} \mathring{\mathring{\vec{\rho}}} = &\begin{bmatrix} b_4 & b_5 & 0 \\ -b_5 & b_4 & b_6 \\ 0 & -b_6 & b_4 \end{bmatrix}\mathring{\vec{\rho}} + \begin{bmatrix} b_7 & b_9 & b_8 \\ -b_9 & b_{10} & b_{11} \\ b_8 & -b_{11} & b_{12} \end{bmatrix}\vec{\rho} \\ &- \frac{\tilde{\mu}_S}{(\tau')^2 l_{SB*}^3}\vec{\rho} - \frac{3\tilde{\mu}_S(\hat{i}_H \cdot \vec{\rho})}{(\tau')^2 l_{SB*}^3}\hat{i}_H + b_{13}\nabla_{\vec{\rho}}\Omega_{CR3BP}, \end{aligned} \tag{9}$$

where $\Omega_{CR3BP} = (1-\mu)/\rho_{Ec} + \mu/\rho_{Mc}$ with,

$$\rho_{Ec} = |\vec{\rho} + \mu\hat{x}|, \quad \rho_{Mc} = |\vec{\rho} - (1-\mu)\hat{x}|, \tag{10}$$

evaluated for fixed Earth and Moon locations within the pulsating-rotating frame. The terms $b_{4-13} = b_{4-13}(\vec{r}_{EM})$ are evaluated with the instantaneous Earth-Moon configuration supplied by the H3BP, e.g., the dimensional distance between the two bodies. While Eq. (9) is rendered with respect to the Hill time, τ, it is possible to reformulate with respect to the pulsating nd time, t. Such an adaptation results in $b_{13} = 1$ and facilitates analytical cancellations between the terms, resulting in,

$$\begin{aligned} \frac{d^2\vec{\rho}}{dt^2} = &\frac{d^2\vec{\rho}}{dt^2}|_{CR3BP} + \begin{bmatrix} b_4 & b_5 - 2 & 0 \\ -b_5 + 2 & b_4 & b_6 \\ 0 & -b_6 & b_4 \end{bmatrix}\frac{d\vec{\rho}}{dt} \\ &+ \frac{3\mu_S}{\rho_S^5}\begin{bmatrix} 0 & 2x_S y_S & 0 \\ 0 & y_S^2 - x_S^2 & y_S z_S \\ 0 & y_S z_S & \rho_S^2 + z_S^2 \end{bmatrix}\vec{\rho}, \end{aligned} \tag{11}$$

where $d^2\vec{\rho}/dt^2|_{CR3BP}$ supplies the acceleration that is identical to the Earth-Moon CR3BP for the same state, $\vec{\rho}$ and $d\vec{\rho}/dt$. A more complete description of the terms in Eqs. (9) and (11) is provided in Park, Sanaga, and Howell [2]. The differences in the HR4BP as derived in two rotating frames, i.e., the uniform-rotating frame and the pulsating-rotating frame, are discussed in Sec. 5 within the context of quasi-periodic extensions for the HR4BP.

Copyright © 2024 by the authors. Published by the IAF, with permission and released to the IAF to publish in all forms.

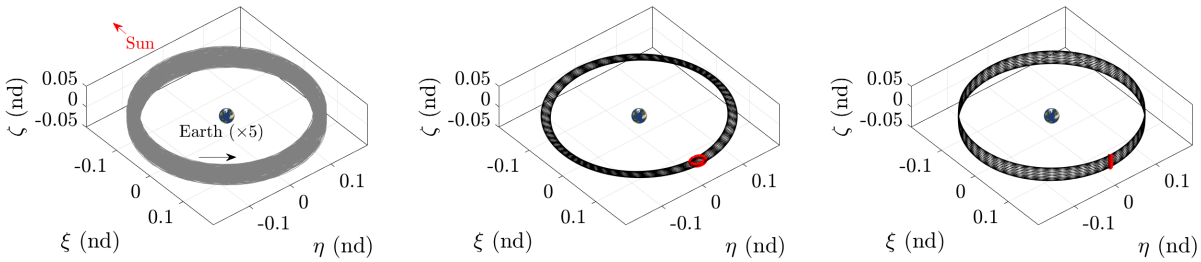

(a) Ephemerides DE440 [6] (b) In-plane H3BP QPO ($\varepsilon \approx 0.0546$) (c) Out-of-plane H3BP QPO ($\iota \approx 5.16^\circ$)

Fig. 3. Lunar motion within the Hill frame described by different structures (the red curves in Figs 3(b) denote 3(c) are invariant curves)

4. Approximating HR3BP 2D-QPOs

Within the general HR4BP framework as depicted in Fig. 2, the instantaneous H3BP solution, $\vec{r}_{EM}(\tau)$, is supplied to evaluate the Sun-Earth-Moon configuration within the HR4BP. Thus, the quasi-periodic extension for the HR4BP involves providing $\vec{r}_{EM}$ that tracks the 2D-QPO behavior within the H3BP, where multiple options exist to approximate such structures. These strategies are compared, highlighting the trade-off between the implementation complexity as well as the accuracy in properly representing the 2D-QPOs.

4.1 Nonlinear QPO: 1D-Fourier series with explicit propagation in the H3BP

In this option, the nonlinear QPOs are first targeted via an algorithm developed in Gómez and Mondelo [7] as well as Olikara and Scheeres [8] (GMOS). The notations in the current investigation generally follow McCarthy [9]. The 2D-QPOs admit angular representation with two sets of angles, $\theta_{lat}, \theta_{lon}$, corresponding to the longitudinal and latitudinal angles, evolving linearly with respect to the independent variable, τ_3. The linear rate correspond to the frequencies, ν_{lat} and ν_{lon}. Then, at a fixed θ_{lon}[†], an invariant curve emerges; the state remains bounded on the curve every stroboscopic time, i.e., passage of 2π in θ_{lon} and $2m\pi$ in τ_3. For the current analysis, $\theta_{lon} = 0$ is leveraged, defined at a location where the average η value is zero with $\xi > 0$, an arbitrary but convenient selection. For instance, the invariant curves are plotted in red within Figs. 3(b) and 3(c). An invariant curve is then governed by the remaining angle, θ_{lat}. It is possible to a leverage 1D-Fourier series representation to approximate this curve, rendering,

$$\vec{u}(\theta_{lat}) \approx e^{i\vec{k}_{lat}\theta_{lat}}\boldsymbol{A}, \tag{12}$$

where $i^2 = \sqrt{-1}$, and

$$\vec{k}_{lat} = \left[-\tfrac{N_{lat}-1}{2} \quad -\tfrac{N_{lat}-1}{2}+1 \quad \ldots \quad \tfrac{N_{lat}-1}{2}\right], \tag{13}$$

a row vector of length N_{lat}, a number of sample points. The complex valued Fourier coefficient matrix $\boldsymbol{A}$ is constructed as $\boldsymbol{A} = \boldsymbol{DU}$ where $\boldsymbol{U}$ is a $(N_{lat}, 6)$ matrix with each row corresponding to the sampled state at evenly placed θ_{lat}. These sample angles are contained in a row vector, $\vec{\theta}_{lat}$. The Discrete Fourier Transform (DFT) matrix $\boldsymbol{D}$ is supplied as,

$$\boldsymbol{D} = \frac{1}{N_{lat}} e^{-i\vec{k}_{lat}^{\intercal}\vec{\theta}_{lat}}, \tag{14}$$

where $\intercal$ denotes a transpose of a vector. The sizes of $\boldsymbol{D}$ and $\boldsymbol{A}$ are (N_{lat}, N_{lat}) and $(N_{lat}, 6)$, respectively. Thus, the six-dimensional invariant curve is parameterized by one angle (θ_{lat}) through Eq. (12). The states on the invariant curve are numerically targeted via enforcing the invariance condition, i.e., after one stroboscopic time, the state rotates on the invariant curve by,

$$\sigma = \text{mod}(2\pi\nu_{lat}/\nu_{lon}, 2\pi), \tag{15}$$

where mod is the modular operator; this quantity is denoted as the rotation number. For the current investigation, $N_{lat} = 25$ is leveraged to target the 2D-QPO. Recall that the monodromy matrix for the LVO predicts two distinct families of 2D-QPOs. Thus, $lat = \varepsilon, \iota$ represent these two families, corresponding to the in-plane and out-of-plane 2D-QPO families. Sample 2D-QPOs are provided in Figs. 3(b) and 3(c), where the state matrix $\boldsymbol{U}$ for each 2D-QPO is supplied in Tables 3 and 4 in Appendix.

Leveraging the 1D-Fourier approximation for the invariant curve, any state on the 2D-QPO is supplied via an

[†]It is possible to leverage a fixed θ_{lat} for defining an invariant curve, e.g., in McCarthy [9]. Depending on the shape of the 2D-QPO, one definition requires less number of terms in the 1D-Fourier series than the other.

Copyright © 2024 by the authors. Published by the IAF, with permission and released to the IAF to publish in all forms.

explicit integration scheme. Assume that for an arbitrary initial epoch, i.e., 0, the initial angles are $\theta_{lon} = 0$ and θ_{lat}. Then, for any epoch τ_3, the state is supplied via,

$$\vec{r}_{EM}(\tau_3) = \vec{\Psi}_0^{\tau_3}(\vec{u}(\theta_{lat})), \tag{16}$$

where $\vec{u}(\theta_{lat})$ is evaluated from Eq. (12) and $\vec{\Psi}_0^{\tau_3}$ is the flow mapping function from the initial epoch to τ_3 under the H3BP dynamics, supplied via any explicit integration scheme. For every $2m\pi$ in τ_3, θ_{lon} completes one full revolution. Thus,

$$\vec{r}_{EM}(\tau_3) = \vec{\Psi}_0^{\tau_3 - 2nm\pi}(\vec{u}(\theta_{lat} + n\sigma)), \tag{17}$$

where n is the number of revolutions in θ_{lon} and σ is evaluated through Eq. (15). Note that this "reset" on the invariant curve is necessary to prevent $\vec{r}_{EM}$ from diverging from the desired 2D-QPO over a longer propagation time in τ_3. In this scheme, the integration ($\vec{\Psi}$) from Eq. (17) is performed simultaneously along with the integration of the HR4BP dynamics as cast in Eqs. (6) or (9). Caution is required for handling $\tau_3 = m\tau$, i.e., the indendent variables for the H3BP and HR4BP are different but uniformly scaled.

4.2 Nonlinear QPO: 2D-Fourier series without propagation

Since the 2D-QPOs allow angular representation with $\theta_{lat}, \theta_{lon}$, approximating them with 2D-Fourier series discards any requirement for any explicit integration and suggests an alternative. The 2D-QPO structures are approximated as follows,

$$\vec{r}_{EM} = \vec{r}_{EM}(\theta_{lat}, \theta_{lon}) \approx e^{i\vec{k}_{lat}\theta_{lat}} \otimes e^{i\vec{k}_{lon}\theta_{lon}} \boldsymbol{A}_{2D}, \tag{18}$$

where $\otimes$ is the Kronecker tensor product. Note that $\vec{k}_{lon}$ is defined similarly as in Eq. (13) with N_{lon} sample points for the longitudinal angle, θ_{lon}. The Kronecker product between the exponential matrices in Eq. (18) results in a $(1, N_{lat}N_{lon})$ vector, multiplied by the Fourier coefficient matrix $\boldsymbol{A}_{2D}$ of a size $(N_{lat}N_{lon}, 6)$. The coefficient matrix is supplied via the DFT matrix,

$$\boldsymbol{D}_{2D} = \frac{1}{N_{lat}N_{lon}} e^{-i\vec{k}_{lat}^{\intercal}\vec{\theta}_{lat}} \otimes e^{-i\vec{k}_{lon}^{\intercal}\vec{\theta}_{lon}}. \tag{19}$$

A $(N_{lat}N_{lon}, 6)$ matrix $\boldsymbol{U}_{2D}$ is constructed that is comprised of states along the 2D-QPO associated with combinations of sampled angles in $\theta_{lat} \in \vec{\theta}_{lat}$ and $\theta_{lon} \in \vec{\theta}_{lon}$. Note that the first N_{lon} rows correspond to a fixed θ_{lat} and varying θ_{lon} values to be consistent with the direction of the tensor product as introduced in Eqs. (18)-(19). Then, $\boldsymbol{A}_{2D} = \boldsymbol{D}_{2D}\boldsymbol{U}_{2D}$ provides the 2D-Fourier coefficients.

The option to avoid explicit integration generally results in a slight degradation of accuracy in approximating the 2D-QPOs. The most notable factor is the number of sample points, N_{lat}, N_{lon}. While larger sample numbers generally lead to more accurate approximation, it involves larger matrix constructions as observed in Eq. (18). For $N_{lat} = N_{lon} = 25$, $\boldsymbol{A}_{2D}$ is constructed for two 2D-QPOs that correspond to in-plane and out-of-plane directions as plotted in Figs. 3(b) and 3(c), respectively. In Fig. 4, the norm of each component for $\boldsymbol{A}_{2D}$ is provided. Figure 4(a) depicts the quantities for the in-plane 2D-QPO from Fig. 3(b), focusing on the ξ-position components. Similarly, Fig. 4(b) corresponds to the 2D-QPO from Fig. 3(c) for the ζ-position components. The plots offer reference visual criteria for selecting suitable N_{lat}, N_{lon} values for proper representation for the 2D-QPOs. The 2D-Fourier series approximation serves as an alternative that potentially requires less overall computation time where the Earth-Moon state vector is evaluated via the closed form 2D-Fourier series. From an initial epoch, 0, associated with $\theta_{lat} = \theta_{lon} = 0$, the state at τ_3 is retrieved as,

$$\vec{r}_{EM}(\tau_3) = \vec{r}_{EM}(\theta_{lat} = \nu_{lat}\tau_3, \theta_{lon} = \nu_{lon}\tau_3), \tag{20}$$

where $\nu_{lat,lon}$ correspond to the frequency for each angle. Then, Eq. (18) is trivially evaluated tor the angles $(\theta_{lat}, \theta_{lon})$. For sample numerical targeting problems within the QHR4BPs, the nonlinear QPO representation with (i) 1D-Fourier + explicit integration ($N_{lat} = 25$) and (ii) 2D-Fourier without explicit integration ($N_{lat} = N_{lon} = 25$) produce nearly identical results.

4.3 Linear QPO

The third option represents a simpler approach to approximate the 2D-QPO with the linear center subspace as governed by the underlying LVO. This strategy is previously explored by Legrand and Scheeres [10] for the out-of-plane QPOs. From Floquet theory, it is possible to express the state transition matrix evaluated between 0 and τ_3 in the following form [11],

$$\Phi(\tau_3, 0) = \mathscr{E}(\tau_3)e^{B\tau_3}\mathscr{E}^{-1}(0), \tag{21}$$

where $\mathscr{E}(0)$ is a 6×6 matrix with the columns corresponding to the five independent complex eigenvectors for the monodromy matrix and a generalized eigenvector for the trivial eigenvalue that exists in the autonomous H3BP. The matrix B corresponds to a block diagonal matrix associated with the eigenvalues of the monodromy matrix, and $\mathscr{E}(\tau_3)$ is a $2m\pi$-periodic matrix. Note that the eigenstructure for the lunar variational periodic orbit admits trivial$\times$center$\times$center, where the two center modes exist in in-plane and out-of-plane directions within the Hill frame. For any of these center subspaces, the Eq. (21)

Copyright © 2024 by the authors. Published by the IAF, with permission and released to the IAF to publish in all forms.

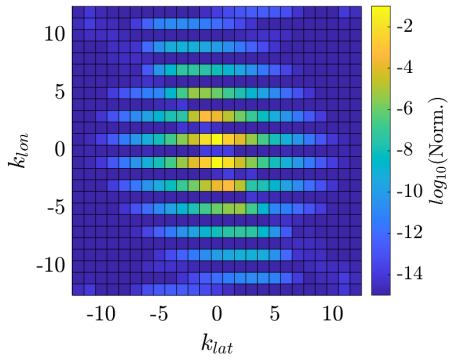

(a) In-plane QPO ξ ($\varepsilon \approx 0.0546$, Fig. 3(b))

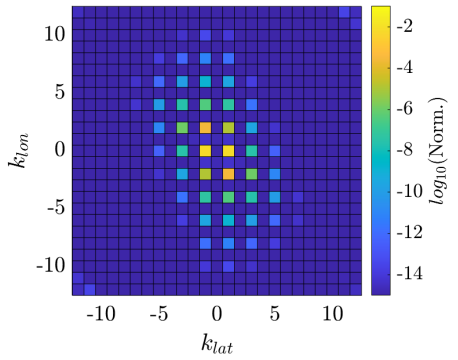

(b) Out-of-plane QPO ζ ($\iota \approx 5.16^\circ$, Fig. 3(c))

Fig. 4. Norm of each component in $\boldsymbol{A}_{2D}$

reduces to,

$$\begin{bmatrix} \delta\vec{r}_{EM} \\ \frac{d\delta\vec{r}_{EM}}{d\tau_3} \end{bmatrix} = \Phi(\tau_3,0)\begin{bmatrix}\vec{f}_1(0) & \vec{f}_2(0)\end{bmatrix} = \begin{bmatrix}\vec{f}_1(\tau_3) & \vec{f}_2(\tau_3)\end{bmatrix}\boldsymbol{C}_L. \tag{22}$$

The variational Earth-Moon state vector is $\delta\vec{r}_{EM}$. The vectors $\vec{f}_{1,2}(0)$ correspond to the real-valued eigenvectors that span the center subspace. For the complex conjugate eigenvectors corresponding to the center subspace, $\vec{e}_{1,2}$, $\vec{f}_1(0) = (\vec{e}_1 + \vec{e}_2)/2$ and $\vec{f}_2(0) = (\vec{e}_1 - \vec{e}_2)/(2i)$ for $i^2 = -1$. For consistency, the first vector, $\vec{f}_1(0)$, is normalized to supply a unit magnitude; the second vector, $\vec{f}_2(0)$, is scaled correspondingly but does not result in a unit magnitude. Note that two different sets of $\vec{f}_{1,2}(0)$ exist for the in-plane and out-of-plane directions. In Eq. (22), the Floquet modes $\vec{f}_{1,2}(\tau_3)$ are $2m\pi$-periodic. The direction cosine matrix $\boldsymbol{C}_L$ is provided as,

$$\boldsymbol{C}_L = \begin{bmatrix} \cos(\sigma\tau_3/(2\pi)) & -\sin(\sigma\tau_3/(2\pi)) \\ \sin(\sigma\tau_3/(2\pi)) & \cos(\sigma\tau_3/(2\pi)) \end{bmatrix}, \tag{23}$$

linking $\vec{f}_{1,2}(0)$ and $\vec{f}_{1,2}(\tau_3)$. The frequencies $\nu_{lat,lon}$ are constructed from the eigenvalues of the monodromy matrix, and σ is evaluated from Eq. (15). Leveraging Eq. (22) and sampling multiple $\vec{f}_{1,2}(\tau_3)$ vectors for $\theta_{lon} \in [0, 2\pi)$, a 1D-Fourier representation is accomplished for each Floquet mode. For the in-plane center subspace, the $\hat{k}_H$-direction position and velocity components are zeros; and $\hat{i}_H - \hat{j}_H$-direction components are zeros for the out-of-plane center subspace. Noting these properties, the Floquet modes are approximated as,

$$\vec{f}_{1,2}(\tau_3) = \vec{f}_{1,2}(\theta_{lon} = \nu_{lon}\tau_3) \approx e^{i\vec{k}_{lon}\theta_{lon}}\boldsymbol{A}_{1,2}, \tag{24}$$

drawing similarities with Eq. (12). While these 1D-Fourier series decay at a fast rate due to the "round" shape of the LVO, for an accurate representation, the length of the vector $\vec{k}_{lon}$ must be greater than one; the vectors $\vec{f}_{1,2}(\tau_3)$ cannot be approximated with one pair of cosine and sine functions. The linear approximation for the invariant curve is constructed trivially from the eigenvectors, $\vec{f}_{1,2}(0)$. For the in-plane center subspace, it is constructed as,

$$\vec{u}(\theta_{lat};\varepsilon) \approx \kappa_e\varepsilon(\vec{f}_1(0)\cos(\theta_{lat}) + \vec{f}_2(0)\sin(\theta_{lat})), \tag{25}$$

where ε is a parameter that approximately tracks the Earth-Moon eccentricity [12]. Assuming that the norm of $\vec{f}_1(0)$ is unity and $\vec{f}_2(0)$ is adjusted correspondingly, κ_e is a constant scalar supplied as $\kappa_e \approx 2.9185$, a value computed from the monodromy matrix. Then, leveraging the 1D-Fourier series for the Floquet modes, any state on the linear variation along the 2D-QPO is represented as,

$$\begin{bmatrix} \delta\vec{r}_{EM}(\theta_{lon},\theta_{lat};\varepsilon) \\ \frac{d\vec{r}_{EM}}{d\tau_3}(\theta_{lon},\theta_{lat};\varepsilon) \end{bmatrix} = \kappa_e\varepsilon\begin{bmatrix}\vec{f}_1(\theta_{lon}) & \vec{f}_2(\theta_{lon})\end{bmatrix} C \begin{bmatrix}\cos(\theta_{lat}) \\ \sin(\theta_{lat})\end{bmatrix}. \tag{26}$$

Then, the Earth-Moon state vector is retrieved by adding $\delta\vec{r}_{EM}$ and $d\delta\vec{r}_{EM}/d\tau_3$ to the reference state on the LVO. Similarly, the out-of-plane 2D-QPO is also constructed as follows,

$$\begin{bmatrix} \delta\vec{r}_{EM}(\theta_{lon},\theta_{lat};\iota) \\ \frac{d\vec{r}_{EM}}{d\tau_3}(\theta_{lon},\theta_{lat};\iota) \end{bmatrix} = \kappa_i\tan(\iota)\begin{bmatrix}\vec{f}_1(\tau_3) & \vec{f}_2(\tau_3)\end{bmatrix} C \begin{bmatrix}\cos(\theta_{lat}) \\ \sin(\theta_{lat})\end{bmatrix}. \tag{27}$$

For a unit-magnitude $\vec{f}_1(0)$ and $\vec{f}_2(0)$ scaled correspondingly, $\kappa_i \approx 2.4761$, and ι corresponds to the approximate inclination of the Moon with respect to the ecliptic [12]. Again, note that $\vec{f}_{1,2}$ are defined distinctly for the in-plane and out-of-plane center subspaces.

The "accuracy" of the linear approximation is nuanced in general. Of course, the approximation is truly correct only in a limiting sense. For $\varepsilon_a, \iota_a > 0$, the nonlinear QPOs may significantly depart from the linear QPOs,

Copyright © 2024 by the authors. Published by the IAF, with permission and released to the IAF to publish in all forms.

rendering the linear representation undesirable. For illustration, nonlinear and linear invariant curves for the QPOs are demonstrated in Fig. 5. The in-plane 2D-QPOs are depicted in Figs. 5(a) and 5(b) for $\varepsilon \approx 0.0546$. The thick lines in the figures correspond to the invariant curves that are constructed with nonlinear (Eq. (12)) and linear (Eq. (25)) methods. The thin lines illustrate sample trajectories that initiate from the invariant curves at $\theta_{lat} = 0$; after one full revolution in θ_{lon}, the trajectory returns to the respective invariant curve, rotated by σ. From the zoomed-out view in Fig. 5(a), it is challenging to differentiate behaviors from the nonlinear and linear QPOs. Upon a closer examination in Fig. 5(b), some deviations are observed. For the particular trajectories emanating from $\theta_{lat} = 0$, a position difference of 8000 km is accrued after one stroboscopic time (synodic lunar month). A similar level of discrepancy between linear and nonlinear 2D-QPOs is observed for the out-of-plane direction as illustrated in Figs. 5(c) and 5(d). Note that while the linear out-of-plane center subspace does not supply any deviation in the in-plane directions, the nonlinear 2D-QPOs evolve in a more complex manner as evident in Fig. 5(d).

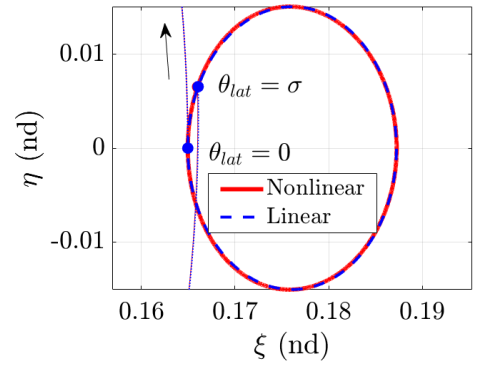

(a) In-plane zoom-out

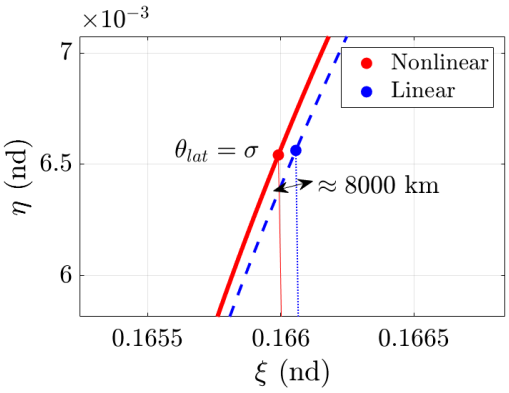

(b) In-plane zoom-in

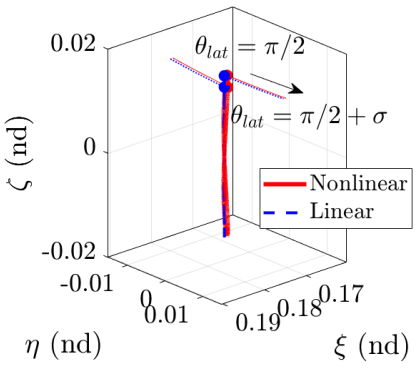

(c) Out-of-plane zoom-out

Fig. 5. Comparison of nonlinear and linear invariant curves

Generally speaking, leveraging the linear 2D-QPO for approximating the nonlinear 2D-QPO requires caution. A sample case is illustrated for the Earth-Moon L_2 9:2 synodic southern halo orbit that is expected to serve as baseline orbit for NASA's Gateway mission [13]. The CR3BP provides a periodic orbit; it evolves into a 2D-QPO within the QHR4BPs due to the 9:2 resonance of the orbital period and synodic lunar month. The initial guess in the CR3BP and the corresponding 2D-QPO within the I-QHR4BP with $\varepsilon \approx 0.0546$ are illustrated in Figs. 6(a) and 6(b). The numerical targeting process for the 2D-QPO within the I-QHR4BP is provided in Park, Sanaga, and Howell [2] and remains out-of-scope for the current investigation. The 2D-QPO construction leverages the nonlinear invariant curve as depicted in red within Fig. 5(a) and serves as a benchmark to assess the linear approximation. Note that the Earth-Moon motion along any linearly approximated 2D-QPO no longer represents a solution within the H3BP. This nuance is notable, as the coherency within the HR4BP is supplied by the fact that the Earth-Moon motion *is* a solution for the H3BP. Depending on the formulation, the lack of coherency may have a varying degree of impact, but it generally degrades the "accuracy" of the analog structures intended to be located. Recall that Eq. (9) provides the HR4BP dynamics within the pulsating-rotating frame, where the b-terms are evaluated with quantities derived from $\vec{r}_{EM}$. These quantities include the acceleration $d^2\vec{r}_{EM}/d\tau_3^2$. As linear approximation for the 2D-QPO is not a solution within the H3BP, two possible options emerge in providing suitable accelerations: (i) evaluate the "osculating" H3BP dynamics from Eq. (5) with $\vec{r}_{EM}$ and $d\vec{r}_{EM}/d\tau_3$ supplied by the linear approximation (Eq. (26)), and (ii) supply the variational acceleration, i.e., $d^2\vec{r}_{EM}/d\tau_3^2$, from differentiating Eq. (26) with respect to τ_3 and adding it to the acceleration along the LVO. Leveraging these two different approximations for the acceleration, 2D-QPOs in the I-QHR4BP are tar-

Copyright © 2024 by the authors. Published by the IAF, with permission and released to the IAF to publish in all forms.

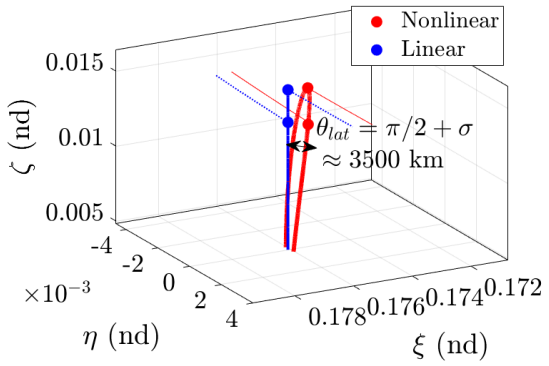

(d) Out-of-plane zoom-in

Fig. 5. Comparison of nonlinear and linear invariant curves

geted with the linear 2D-QPOs for the H3BP. These structures are juxtaposed with the 2D-QPO in Fig. 6(b) that utilizes a nonlinear 2D-QPO. The position crossings within the pulsating-rotating frame are recorded with $z = 0$ and $dz/d\tau > 0$ in Fig. 7. It is evident that linear (ii) approach amplifies the lack of coherency for the Earth-Moon motion. The targeting process fails around $\varepsilon \approx 0.02$ to produce a well-defined 2D-QPO analog for the 9:2 halo orbit; the cyan dots are associated with the last 2D-QPO that is able to converge. While the linear (ii) method performs significantly better than linear (i) formulation, it displays some deviation from the structure produced from the nonlinear 2D-QPO. Due to the nuances associated with the coherency, i.e., the HR4BP leverages the Earth-Moon motion as a *solution* within the H3BP, where the linear approximation for the H3BP 2D-QPOs requires extra caution. Note that in deriving the HR4BP in the uniform-rotating frame [3], it is assumed that the Earth-Moon motion follows the H3BP solution; thus, it leverages the linear (i) formulation by default when substituting $\vec{r}_{EM}$ from the linearly approximated 2D-QPOs.

5. Frame Rotations for Two Rotating Frames in the HR4BP

Recall that the general HR4BP leverages dynamics as formulated in two rotating frames: the uniform-rotating frame and the pulsating-rotating frame. These frames offer distinct advantages and disadvantages in terms of (i) ease of implementation, (ii) sensitivities in the numerical targeting process, and (iii) visualization. Thus, it is imperative to properly define a rotation scheme between these two frames for a versatile quasi-periodic extension for the HR4BP.

The rotation starts from describing the direction cosine

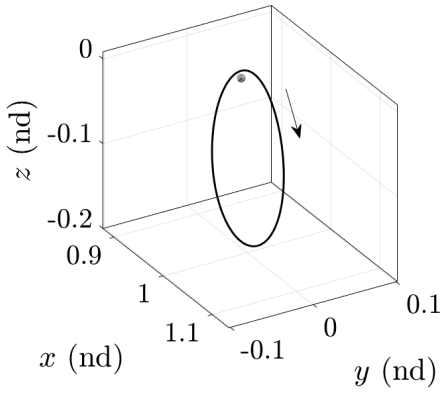

(a) CR3BP

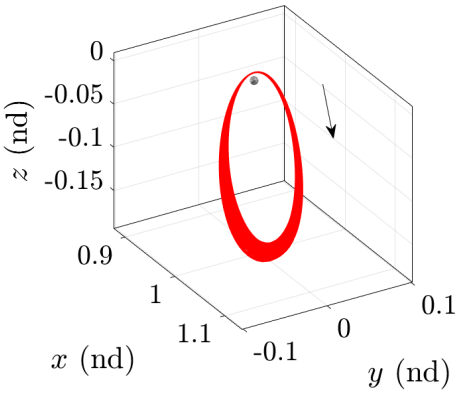

(b) I-QHR4BP ($\varepsilon \approx 0.0546$)

Fig. 6. 9:2 L_2 southern halo orbit within pulsating-rotating frame

matrix between the two frames. The matrix is constructed as,

$$\boldsymbol{C} = \begin{bmatrix} \hat{x} & \hat{y} & \hat{z} \end{bmatrix}, \tag{28}$$

where $\hat{x} - \hat{y} - \hat{z}$ are evaluated in terms of the $\hat{x}_* - \hat{y}_* - \hat{y}_*$ vectors as follows,

$$\hat{x} = \frac{\vec{\rho}_{EM*}}{|\vec{\rho}_{EM*}|}, \; \hat{z} = \frac{\vec{\rho}_{EM*} \times \mathring{\vec{\rho}}^{I}_{EM*}}{|\vec{\rho}_{EM*} \times \mathring{\vec{\rho}}^{I}_{EM*}|}, \; \hat{y} = \hat{z} \times \hat{x}. \tag{29}$$

Recall that $\vec{\rho}_{EM*} = x_{EM*}\hat{x}_* + y_{EM*}\hat{y}_* + z_{EM*}\hat{z}_*$ from Eq. (4). The derivative of a vector as observed from an inertially fixed observer is denoted with the superscript I, resulting in,

$$\mathring{\vec{\rho}}^{I}_{EM*} = \mathring{\vec{\rho}}_{EM*} + (1+m)\hat{z}_* \times \vec{\rho}_{EM*}, \tag{30}$$

with $\mathring{\vec{\rho}}_{EM*} = \mathring{x}_{EM*}\hat{x}_* + \mathring{y}_{EM*}\hat{y}_* + \mathring{z}_{EM*}\hat{z}_*$. Then, the nd spacecraft position vectors in both frames are related

Copyright © 2024 by the authors. Published by the IAF, with permission and released to the IAF to publish in all forms.

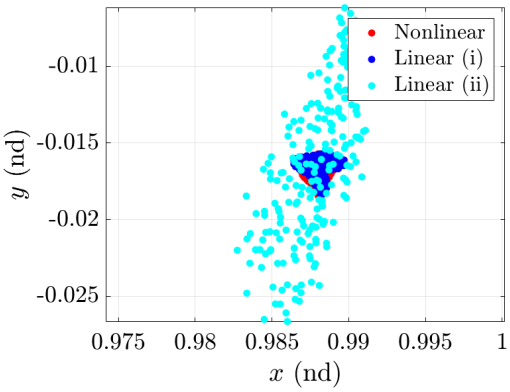

(a) Zoomed-out view

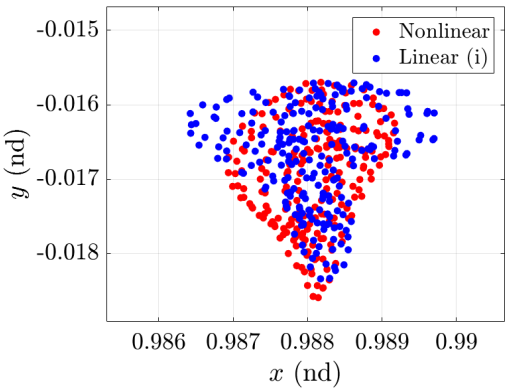

(b) Zoomed-in view

Fig. 7. Crossings at $z = 0$, $\mathring{z} > 0$ for 2D-QPO 9:2 L_2 halo counterpart constructed with nonlinear and linear H3BP 2D-QPOs

through,

$$\vec{\rho}_* = \frac{l}{l_*}\boldsymbol{C}\vec{\rho}, \tag{31}$$

noting that the uniform and pulsating rotating frames leverage the average and instantaneous Earth-Moon distance, i.e., l_*, l, as the dimensionalization quantities, respectively. Then, the velocities are related via,

$$\mathring{\vec{\rho}}_* = (\frac{\mathring{l}}{l_*}\boldsymbol{C} + \frac{l}{l_*}\mathring{\boldsymbol{C}}^I)\vec{\rho} + \frac{l}{l_*}\boldsymbol{C}\mathring{\vec{\rho}}, \tag{32}$$

with the Earth-Moon distance evaluated as,

$$l = |\vec{\rho}_{EM*}|l_*, \quad \mathring{l} = l\left(\vec{\rho}_{EM*}\cdot\mathring{\vec{\rho}}_{EM*}\right). \tag{33}$$

The derivative of the direction cosine matrix results in,

$$\mathring{\boldsymbol{C}}^I = \begin{bmatrix} \mathring{\hat{x}}^I & \mathring{\hat{y}}^I & \mathring{\hat{z}}^I \end{bmatrix}, \tag{34}$$

where the derivatives for the unit vectors are evaluated as,

$$\mathring{\hat{x}}^I = \frac{\mathring{\vec{\rho}}^I_{EM*}}{|\vec{\rho}_{EM*}|} - \frac{\vec{\rho}_{EM*}\mathring{l}}{|\vec{\rho}_{EM*}|^2 l_*} \tag{35}$$

$$\mathring{\hat{z}}^I = \frac{1}{h}\left(\vec{\rho}_{EM*}\times\mathring{\vec{\rho}}^I_{EM*}\right) - \frac{\mathring{h}}{h^2}\left(\vec{\rho}_{EM*}\times\mathring{\vec{\rho}}^I_{EM*}\right) \tag{36}$$

$$\mathring{\hat{y}}^I = \mathring{\hat{z}}\times\hat{x} + \hat{z}\times\mathring{\hat{x}}, \tag{37}$$

with $h = |\vec{\rho}_{EM*}\times\mathring{\vec{\rho}}^I_{EM*}|$ and $\mathring{h} = (\vec{\rho}_{EM*}\times\mathring{\mathring{\vec{\rho}}}^I_{EM*})\cdot\hat{z}$. The relative acceleration vector for the Earth-Moon system is,

$$\begin{aligned}\mathring{\mathring{\vec{\rho}}}^I_{EM*} = {} & (\mathring{\mathring{x}}_{EM*} - (1+m)\mathring{y}_{EM*})\hat{x}_* \\ & + (\mathring{\mathring{y}}_{EM*} + (1+m)\mathring{x}_{EM*})\hat{y}_* \\ & + \mathring{\mathring{z}}_{EM*}\hat{z}_* + (1+m)\hat{z}_*\times\mathring{\vec{\rho}}_{EM*}.\end{aligned} \tag{38}$$

Then, the state vectors in both frames are related via the following matrix form,

$$\begin{bmatrix}\vec{\rho}_* \\ \mathring{\vec{\rho}}_*\end{bmatrix} = \frac{1}{l_*}\begin{bmatrix} l\boldsymbol{C} & \boldsymbol{0}_{3\times3} \\ \mathring{l}\boldsymbol{C} + l\mathring{\boldsymbol{C}}^I & l\boldsymbol{C}\end{bmatrix}\begin{bmatrix}\vec{\rho} \\ \mathring{\vec{\rho}}\end{bmatrix}, \tag{39}$$

concluding the derivations. The rotation is validated for a sample initial state as included in Table 1. For the Earth-Moon state vector within the Hill frame as in Table 1b, the initial spacecraft state vectors in two rotating frames are related via Eq. (39). These initial states are then propagated in the respective reference frames independently leveraging the corresponding equations of motion, i.e., Eqs. (6) and (9). These trajectories are plotted in their respective rotating frames as in Fig. 8. Then, each trajectory is rotated into the other frame to validate the dynamics in both frames as well as the rotation scheme between them. These two frames and their respective formulations for HR4BP represent distinct options for propagation as well as visualization.

Both frames supply unique advantages and disadvantages. The uniform-rotating frame facilitates a straightforward implementation of the QHR4BP; upon producing the H3BP 2D-QPO solution, it is supplied to the Eq. (6) without additional steps. However, due to the nature of the *uniformly* rotating frame, any numerical targeting process as well as visualization face challenges as discussed in Park, Sanaga, and Howell [2]. For illustration, consider the L_2 counterpart within the two QHR4BPs with $\varepsilon \approx 0.0546$ (I-QHR4BP) and $\iota \approx 5.16^\circ$ (O-QHR4BP) as depicted in Fig. 9. While the CR3BP supplies a fixed L_2 equilibrium point, the counterpart inherits the frequencies of the dynamical model, expected to result in 2D-QPOs within the QHR4BPs. Indeed, the 2D-QPOs constructed within the uniform-rotating frame demonstrate this behavior as evident from Figs. 9(a) and 9(b).

Copyright © 2024 by the authors. Published by the IAF, with permission and released to the IAF to publish in all forms.

Table 1. Sample spacecraft state in the uniform- and pulsating-rotating frame for a Earth-Moon state in Hill frame

(a) Spacecraft state ($\vec{\rho}_*$, $\vec{\rho}$)

state	Uniform-Rotating Frame	Pulsating-Rotating Frame
x	1.011	1.079529411613892
y	0	0.050538991847947
z	-0.049	-0.040554358228579
$\mathring{x}$	0	0.049202308670500
$\mathring{y}$	-0.16	-0.340319947080306
$\mathring{z}$	0	0.085725045752616

(b) Earth-Moon state ($\vec{r}_{EM}, d\vec{r}_{EM}/d\tau_3$)

state	Hill Frame
ξ	0.165846214243881
η	-0.00719127309462785
ζ	-0.00115830363326785
$d\xi/d\tau_3$	0.0438253205343869
$d\eta/d\tau_3$	2.36105433672951
$d\zeta/d\tau_3$	-0.221638631662460

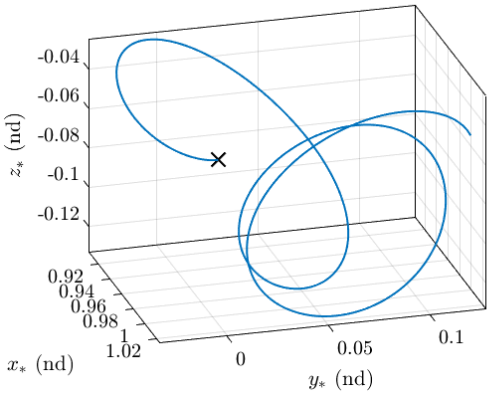

(a) Uniform-Rotating Frame, propagated with Eq. (6)

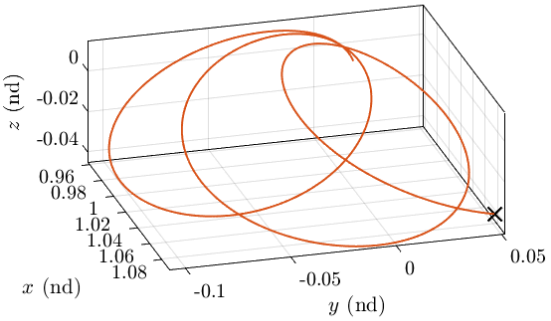

(b) Pulsating-Rotating Frame, propagated with Eq. (9)

Fig. 8. Sample state propagation in the uniform- and pulsting-rotating frame. Black 'x' corresponds to the initial state in both the frames

However, the equivalent structures within the pulsating-rotating frame supplies an equilibrium L_2 point. Within the uniform-rotating frame, depending on the complexity of Earth-Moon motion along the H3BP 2D-QPO, the motion for the spacecraft may be exaggerated as compared to the behaviors within the pulsating-rotating frame. The fixed-point L_2 within the pulsating-rotating frame is confirmed via multiple ways: (i) rotation of the structures via Eq. (39), (ii) numerical evaluation of the pulsating-rotating frame HR4BP dynamics from Eq. (9), and (iii) analytical observation from an alternative representation for the HR4BP within the pulsating-rotating frame in Eq. (11). While numerical targeting schemes within the QHR4BPs may be conducted within the uniform-rotating frame, continuation along the H3BP 2D-QPOs, e.g., varying ε, sometimes faces extra numerical challenges as the spacecraft state $\vec{\rho}_*$ changes significantly from the previous model to adjust the $\vec{\rho}_*$ with respect to the moving celestial bodies, e.g., the Moon. For this reason, the current analysis mainly adopts the pulsating-rotating frame for visualization as well as numerical targeting process.

6. 3D QPO: Evolving Frequencies and Geometries

In this section, the in-plane and out-of-plane center modes are combined, supplying a nonlinear 3D-QPO for the Earth-Moon motion as described within the H3BP. The 3D-QPO targeting process follows McCarthy [9]. For a fixed angle $\theta_{lon} = 0$, an invariant *surface* emerges, parameterized by two angles, θ_ε and θ_ι.

$$\vec{U}(\theta_\varepsilon, \theta_\iota) \approx e^{i\vec{k}_\varepsilon \theta_\varepsilon} \otimes e^{i\vec{k}_\iota \theta_\iota} \boldsymbol{A}_{2D}, \tag{40}$$

drawing similarities with Eq. (18) that is leveraged in approximating the 2D-QPO. In the current analysis, $N_\varepsilon = N_\iota = 11$; this combination results in 121 sampled points on the invariant surface that generally allows rapid construction of the 3D-QPO[‡]. The rotation matrix is defined as,

$$\boldsymbol{R}_{-\sigma_\varepsilon,-\sigma_\iota} = \boldsymbol{D}_{2D}^{-1} \left(\mathrm{d}(e^{-i\vec{k}_\varepsilon \sigma_\varepsilon}) \otimes \mathrm{d}(e^{-i\vec{k}_\iota \sigma_\iota}) \right) \boldsymbol{D}_{2D}, \tag{41}$$

where $\mathrm{d}(\vec{\cdot})$ is a diagonal matrix with the components supplied by the vector. The DFT matrix, $\boldsymbol{D}_{2D}$ is defined anal-

[‡]Upon locating a desired structure, N_ε, N_ι may be refined to supply a more accurate 3D-QPO.

Copyright © 2024 by the authors. Published by the IAF, with permission and released to the IAF to publish in all forms.

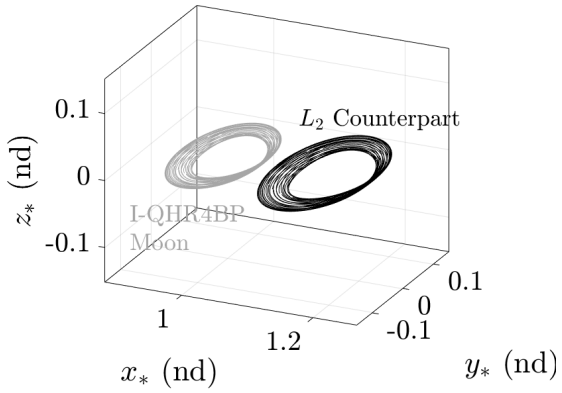

(a) Uniform-rotating frame, in-plane

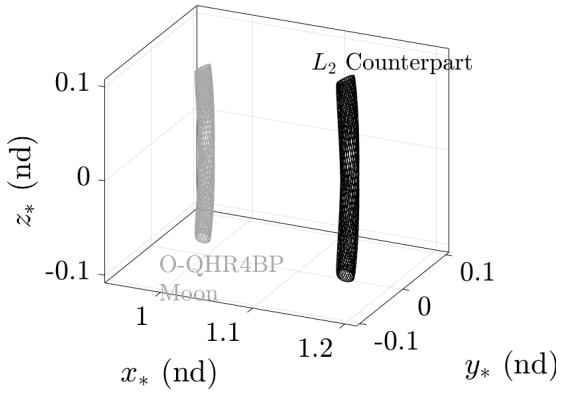

(b) Uniform-rotating frame, out-of-plane

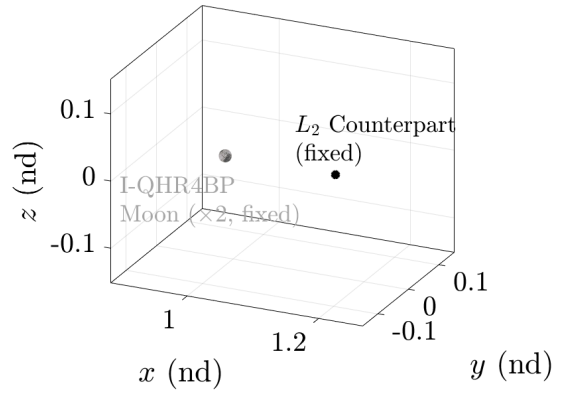

(c) Pulsating-rotating frame, in-plane

Fig. 9. L_2 counterparts within QHR4BPs in two different frames (in-plane: $\varepsilon \approx 0.0546$, out-of-plane: $\iota \approx 5.16^\circ$

ogous to Eq. (19). Then, the invariance condition is constructed as,

$$\boldsymbol{R}_{-\sigma_\varepsilon,-\sigma_\iota}\vec{\Psi}_0^{2m\pi}(\vec{u}(\theta_\varepsilon,\theta_\iota))-\vec{u}(\theta_\varepsilon,\theta_\iota)=\vec{0}, \tag{42}$$

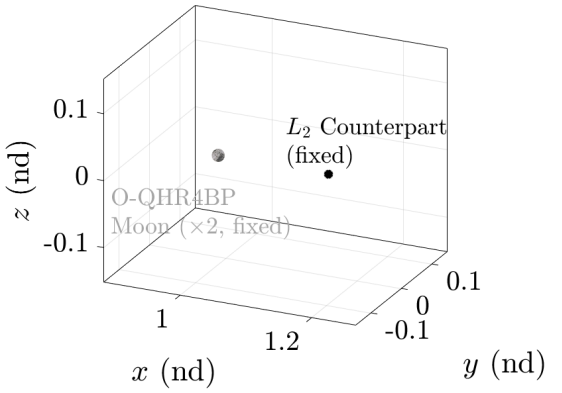

(d) Pulsating-rotating frame, out-of-plane

Fig. 9. L_2 counterparts within QHR4BPs in two different frames (in-plane: $\varepsilon \approx 0.0546$, out-of-plane: $\iota \approx 5.16^\circ$

where $\vec{\Psi}_0^{2m\pi}$ is a stroboscopic mapping function within the H3BP, propagating each initial state from $\theta_{lon}=0$ to $\theta_{lon}=2\pi$. The invariance condition leverages the fact that every stroboscopic time, the state returns to the invariant surface but with rotated angles in $\theta_{\varepsilon,\iota}$ by $\sigma_{\varepsilon,\iota}$. In total, $N_\varepsilon N_\iota$-$\vec{u}$ vectors are numerically targeted that satisfy Eq. (42).

The initial guess for the invariant surface, i.e., Eq. (40), is provided via the center subspaces of the monodromy matrix for the LVO. The nonlinear 3D-QPOs exist as a two-parameter family for a fixed longitudinal period of $2m\pi$. In the current analysis, the rotation numbers $\sigma_{\varepsilon,\iota}$ are adjusted to evolve the two-parameter family. The rotation numbers are related to the frequencies as,

$$\frac{\nu_{\varepsilon,\iota}}{\nu_{lon}}=\sigma_{\varepsilon,\iota}+1. \tag{43}$$

In Fig. 10(a), the horizontal and vertical axes illustrate the ratios $\nu_{\varepsilon,\iota}/\nu_{lon}$, respectively; each point on the 2D-plane represents a 3D-QPO associated with a distinct $\nu_{\varepsilon,\iota}$ combination. The blue star in Fig. 10(a) is the information from the monodromy for the LVO. Initiating from this point, generally, the nonlinear 3D-QPOs evolve with increasing $\nu_{\varepsilon,\iota}/\nu_{lon}$ ratios. The colormap illustrates the approximate eccentricity, ε, corresponding to the nonlinear 3D-QPO targeted via the invariance condition from Eq. (42). The approximate eccentricity is constructed as,

$$\varepsilon \approx \left(\xi(\theta_\varepsilon,\theta_\iota=0)_{max}-\xi(\theta_\varepsilon,\theta_\iota=0)_{min}\right)/c_\varepsilon, \tag{44}$$

where c_ε is a constant derived from m, $c_\varepsilon \approx 0.4084$ [12, 2]. The angle $\theta_\iota=0$ is defined with a minimum mean ζ-excursion on the invariant surface. The approximate in-

Copyright © 2024 by the authors. Published by the IAF, with permission and released to the IAF to publish in all forms.

clination, ι, is constructed via,

$$\iota \approx \arctan((\zeta(\theta_\varepsilon, \theta_\iota)_{max} - \zeta(\theta_\varepsilon, \theta_\iota)_{min})/c_\iota), \qquad (45)$$

for a constant $c_\iota \approx 0.3439$. These values are supplied based on the linear center subspace and serve as reference geometric characteristics for each 3D-QPO. The contour plot for the approximate inclination values is depicted in Fig. 10(b). Note that the black line in Fig. 10(a) corresponds to the boundary for the 2D-QPO; to the left of the line, the 3D-QPOs collapse to 2D-QPOs associated with $\iota_a = \zeta = 0$.

Within the range of the frequencies for $\nu_{\varepsilon,\iota}$, the approximate eccentricity and inclination values, i.e., (ε, ι), demonstrate nearly linear behavior as notable from the contour plots, characterized by straight lines. However, the 3D-QPOs evolve with different frequencies as opposed to the underlying LVO and the 2D-QPOs. For example, consider the red star within Fig. 10(a), corresponding to $\varepsilon \approx 0.055$ with $\iota \approx 0$, tracking a 2D-QPO. A similar value of ε within the 3D-QPO family is supplied by different combinations of ε, ι, allowing the frequencies to evolve. One option is illustrated as the black star in Figs. 10(a) and 10(b). The location is selected based on the frequency information directly retrieved from the lunar ephemerides DE440 [1]. Note that the frequency ν_ε deviates from the linear approximation (blue star) as well as the 2D-QPO (red star) in Fig. 10(a).[§] The 3D-QPO corresponding to the black star is illustrated in Fig. 10(c) within the Hill frame. Note that this 3D-QPO now approximates the perturbations in both in-plane and out-of-plane with both suitable frequencies and geometries as compared to the lunar ephemerides (Fig. 3(a)).

The current analysis for the 3D-QPOs in the H3BP offers potential applications in two distinct fields. In the realm of dynamical astronomy, providing QPOs within the H3BP revisits Hill and Brown's lunar theory, now utilizing modern computational tools and dynamical systems theory. This approach enables a straightforward approximation of the lunar ephemerides. As illustrated in Fig. 10, characterizing the two-dimensional family of 3D-QPOs also offers a global assessment of possible configurations for the Sun-Earth-Moon system, an approach that potentially applies to other systems as well. From an astrodynamics perspective, the H3BP 3D-QPOs serve as the basis for the Three-Dimensional Quasi-Hill Restricted Four-Body Problem (3D-QHR4BP), leveraging the common HR4BP framework as illustrated in Fig. 2. Thus, a quasi-periodic model that incorporates three incommensurate frequencies is supplied that serves as a refined model to further bridge the gap between the CR3BP and the HFEM in the cislunar domain. Also, any member within the two-parameter 3D-QPO family from Fig. 10 serves as an "intermediate" step between the periodic HR4BP (blue star in Fig. 10(a) to any desired 3D-QHR4BP (black star in Fig. 10(a)), providing a adaptable continuation strategy between lower- to higher-fidelity models. While incorporating multiple frequencies is a non-trivial task, the general HR4BP framework and the 2D/3D-QPO structures provide capabilities to *selectively* introduce perturbing frequencies with arbitrary magnitudes.

Focusing on the astrodynamics application, a sample structure, the 9:2 southern halo orbit, is refined within the 3D-QHR4BP and compared with analogs in other models. While the 9:2 orbit is expected to evolve into a 3D-QPO within the 3D-QHR4BP, the exact Hamiltonian structure is not targeted in the current analysis to avoid the computational costs. Rather, a long-term (20 years) continuous solution is supplied without boundary constraints, a process that is typically adopted for the HFEM analogs (Fig. 11(d) and in Zimovan-Spreen et al. [14]). The geometry of the structures is analyzed within the pulsating-rotating frame (Fig. 1(c)); a hyperplane is constructed at $z = 0, \dot{z} > 0$, recording the position crossing on the $\hat{x} - \hat{y}$ plane as illustrated in Fig. 11. Nine colors correspond to nine different returns to the hyperplane, a trait supplied by the synodic resonance ratio of the orbit. The first two plots in Figs. 11(a) and 11(b) are the crossings along the 2D-QPOs targeted within the two QHR4BPs that incorporate the eccentricity (in-plane) and inclination (out-of-plane) (recreated from Park, Sanaga, and Howell [2]). The HFEM result is depicted in Fig. 11(d), where a more complex behavior is observed; overall, however, the shapes of the sections as found from the I-QHR4BP (Fig. 11(a)) are maintained with perturbations. These additional components are further represented within the 3D-QHR4BP, where the crossings now evolve in terms of both the eccentricity and inclination simultaneously as in Fig. 11(c); the crossings appear to be a convolution of the geometries from Figs. 11(a) and 11(b) as expected. The H3BP 3D-QPO in the black star within Fig. 10(a) is leveraged as representing the desired 3D-QHR4BP. A continuation strategy is utilized that originates from the HR4BP resonant periodic orbit (blue star) and terminates at the black star in Fig. 10(a) with multiple steps. Thus, a smooth transition is achieved between the HR4BP and 3D-QHR4BP; the analog within the desired 3D-QHR4BP then provides further insights into the complexity of the HFEM analogs.

[§] Gutzwiller [5] explains the change of the linear frequency (blue star) to the HFEM frequency (black star) as an externally driven parametric oscillator, where the frequency of one mode, e.g., ν_ε, is a function of other frequencies, e.g., ν_ι.

Copyright © 2024 by the authors. Published by the IAF, with permission and released to the IAF to publish in all forms.

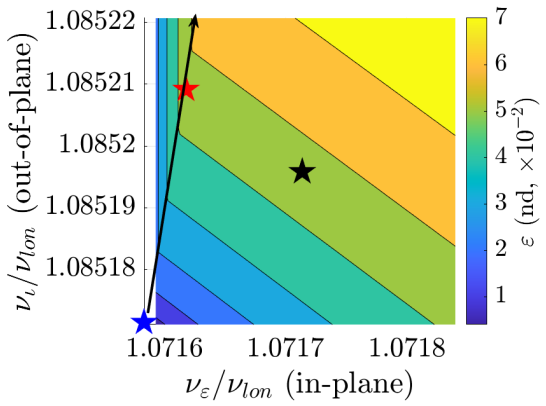

(a) Contour plot for ε

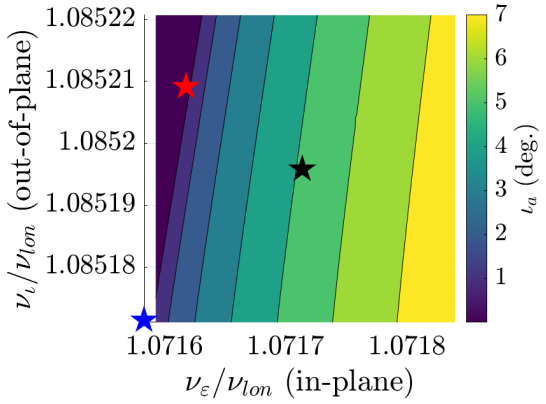

(b) Contour plot for ι

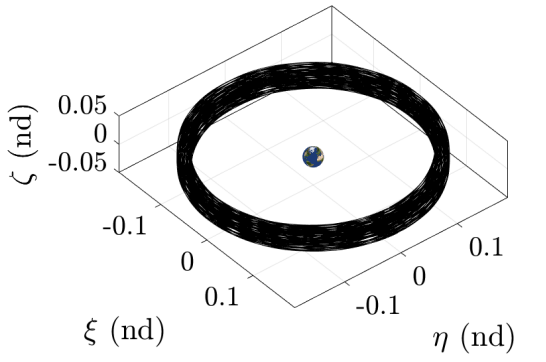

(c) 3D-QPO at the black star in Figs. 10(a) and 10(b)

Fig. 10. The two-parameter H3BP 3D-QPO family

7. Concluding Remarks

The quasi-periodic extensions for the Hill Restricted Four-Body Problem (HR4BP) are further analyzed within the context of the cislunar dynamical environment. Two parallel components are identified that constitute the general HR4BP framework: (i) the H3BP that models the Sun-Earth-Moon configuration and (ii) the HR4BP component that models the restricted four-body problem describing the evolution for the spacecraft. Within this context, multiple strategies exist in approximating the H3BP 2D-Quasi-Periodic Orbits (QPOs) that serve as the basis for extending the HR4BP to include two incommensurate frequencies. Two rotating frames are investigated that result in different capabilities in terms of complexity, targeting, and visualization. Lastly, the 3D-QPOs within the H3BP are supplied that facilitate the extension of the HR4BP to include three incommensurate frequencies, resulting in the Three-Dimensional Quasi-Hill Restricted Four-Body Problem (3D-QHR4BP). The capability of the new model is highlighted for a sample Earth-Moon trajectory, i.e., the L_2 9:2 halo orbit.

Acknowledgements

Beom Park would like to thank Kwanjeong Educational Foundation for the financial support and Korea Aerospace Research Institute for the travel grant through International Space Education Board. Rohith Reddy Sanaga would like to acknowledge the Department of Computer Science-Purdue University. Portions of this work are supported by Purdue University and NASA Johnson Space Center.

References

[1] Gerard Gómez, Josep J Masdemont, and Josep-Maria Mondelo. Solar system models with a selected set of frequencies. *Astronomy & Astrophysics*, 390(2):733–749, 2002. doi:10.1051/0004-6361:20020625.

[2] Beom Park, Rohith Reddy Sanaga, and Kathleen C. Howell. A Frequency-Based Hierarchy of Dynamical Models in Cislunar Space: Leveraging Periodically and Quasi-Periodically Perturbed Models. *PREPRINT (Version 1) available at Research Square*, 2024. doi:10.21203/rs.3.rs-4822764/v1.

[3] Daniel J Scheeres. The Restricted Hill Four-Body Problem with Applications to the Earth-Moon-Sun system. *Celestial Mechanics and Dynamical Astronomy*, 70:75–98, 1998. doi:10.1023/A:1026498608950.

[4] Beom Park and Kathleen C Howell. Assessment of dynamical models for transitioning from the Circular Restricted Three-Body Problem to an ephemeris model with applications. *Celestial Mechanics and Dynamical Astronomy*, 136(6), 2024. doi:10.1007/s10569-023-10178-9.

Copyright © 2024 by the authors. Published by the IAF, with permission and released to the IAF to publish in all forms.

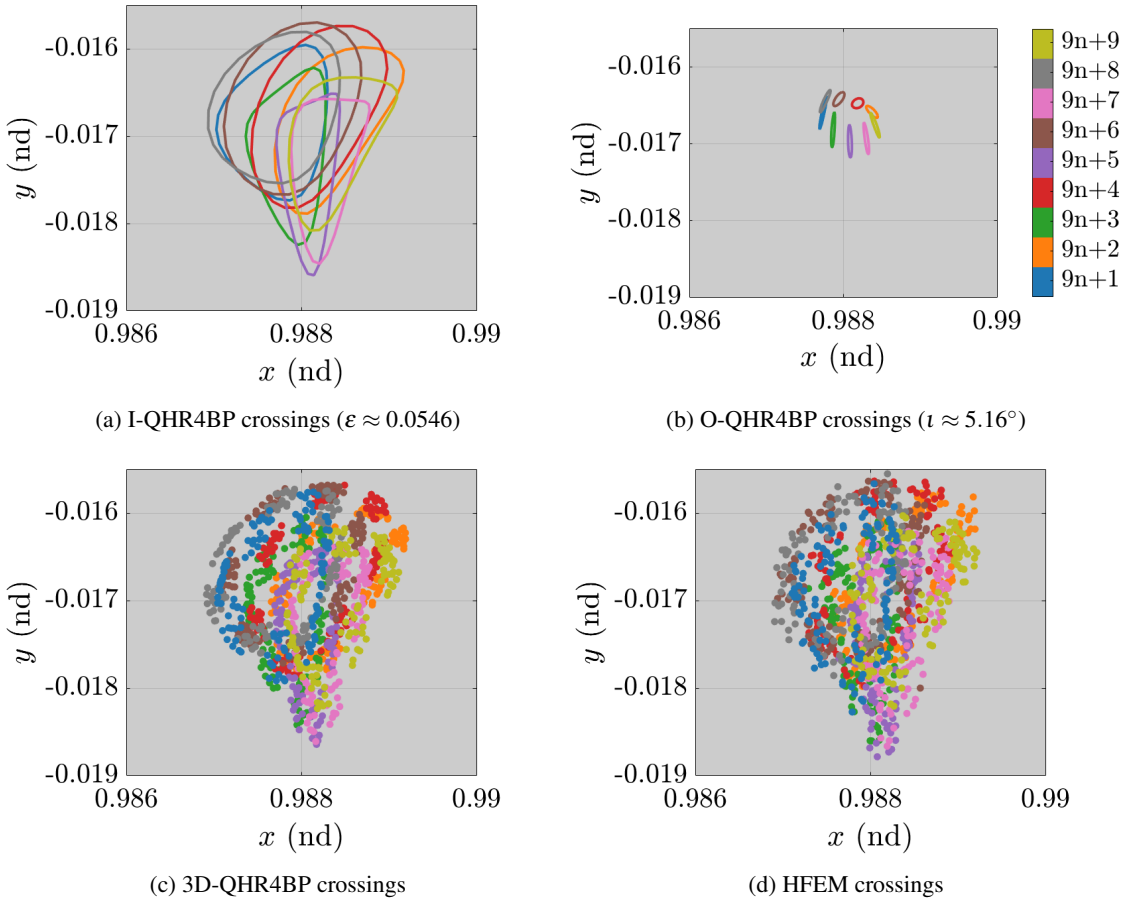

(a) I-QHR4BP crossings ($\varepsilon \approx 0.0546$)

(b) O-QHR4BP crossings ($\iota \approx 5.16°$)

(c) 3D-QHR4BP crossings

(d) HFEM crossings

Fig. 11. L_2 southern 9:2 halo orbit: geometry and crossings at $z = 0$, $\mathring{z} > 0$ (some plots are recreated from Park, Sanaga, and Howell [2])

[5] Martin C Gutzwiller. Moon-Earth-Sun: The oldest three-body problem. *Reviews of Modern Physics*, 70(2):589–639, 1998. doi:10.1103/RevModPhys.70.589.

[6] Ryan S Park, William M Folkner, James G Williams, and Dale H Boggs. The jpl planetary and lunar ephemerides de440 and de441. *The Astronomical Journal*, 161(3):105, 2021. doi:10.3847/1538-3881/abd414.

[7] G. Gómez and J.M. Mondelo. The dynamics around the collinear equilibrium points of the rtbp. *Physica D: Nonlinear Phenomena*, 157(4):283–321, 2001. ISSN 0167-2789. doi:10.1016/S0167-2789(01)00312-8.

[8] Zubin P Olikara and Daniel J Scheeres. Numerical method for computing quasi-periodic orbits and their stability in the restricted three-body problem. *Advances in the Astronautical Sciences*, 145(911-930):911–930, 2012.

[9] Brian McCarthy. *Cislunar trajectory design methodologies incorporating quasi-periodic structures with applications*. Ph.D. Dissertation, Purdue University, U.S., 2022. doi:10.25394/PGS.19678857.v1.

[10] Adrien P Legrand and Daniel J Scheeres. The inclined Hill restricted four-body problem: derivation and applications. In *AAS/AIAA Astrodynamics Specialist Conference, Broomfield, Colorado, August 11-15, 2024.*, 2024.

[11] Dale Williams. Dynamics of long-term orbit maintenance strategies in the circular restricted three body problem. Master's thesis, Purdue University, U.S., 2024. doi:10.25394/PGS.25639269.v1.

[12] George Howard Darwin. *The Scientific Papers of Sir George Darwin: Supplementary*

Copyright © 2024 by the authors. Published by the IAF, with permission and released to the IAF to publish in all forms.

Volume. Cambridge Library Collection - Physical Sciences. Cambridge University Press (Original work published in 1916), 2009/1916. doi:10.1017/CBO9780511703515.

[13] Emily M Zimovan-Spreen, Kathleen C Howell, and Diane C Davis. Near rectilinear halo orbits and nearby higher-period dynamical structures: orbital stability and resonance properties. *Celestial Mechanics and Dynamical Astronomy*, 132(5):28, 2020. doi:10.1007/s10569-020-09968-2.

[14] Emily M Zimovan-Spreen, Stephen T Scheuerle, Brian P Mccarthy, Diane C Davis, and Kathleen C Howell. Baseline orbit generation for near rectilinear halo orbits. In *AAS/AAIA Astrodynamics Specialist Conference*, number AAS 23-268, 2023.

Copyright © 2024 by the authors. Published by the IAF, with permission and released to the IAF to publish in all forms.

Appendix: Initial Conditions for the LVO and Sample 2D-QPOs within the HR3BP

Table 2. Initial condition for the LVO ($\zeta = d\zeta/d\tau_3 = 0$), $m = 8.084893380831200e-02$

ξ	η	$d\xi/d\tau_3$	$d\eta/d\tau_3$
1.760970177183320e-01	0	0	2.222954511784983e+00

Table 3. Invariant curve for in-plane 2D-QPO at $\varepsilon_a \approx 0.0546$ ($\zeta = d\zeta/d\tau_3 = 0$)

k	ξ	η	$d\xi/d\tau_3$	$d\eta/d\tau_3$
1	1.649471037033227e-01	1.242028507943572e-07	-7.934305660149587e-07	2.387182932436084e+00
2	1.652757757966211e-01	3.739522750313633e-03	-2.376997302887450e-02	2.381426960033573e+00
3	1.662455643235383e-01	7.246948243586081e-03	-4.539832754295506e-02	2.364689050275171e+00
4	1.678076136068717e-01	1.030452296455364e-02	-6.308123690122808e-02	2.338465782571995e+00
5	1.698799752757207e-01	1.272160961997992e-02	-7.558800446887907e-02	2.304979348045149e+00
6	1.723482817677429e-01	1.434629413245083e-02	-8.234837613168081e-02	2.266862370786354e+00
7	1.750688541837658e-01	1.507470259584826e-02	-8.339600134043695e-02	2.226852456812197e+00
8	1.778751172316812e-01	1.485777915474438e-02	-7.922025090986035e-02	2.187552526227766e+00
9	1.805874078035917e-01	1.370513602753855e-02	-7.058882455474924e-02	2.151275414040267e+00
10	1.830254772023310e-01	1.168554216001360e-02	-5.838976677104232e-02	2.119962780515571e+00
11	1.850224101866764e-01	8.923674840592777e-03	-4.351864483330420e-02	2.095155716257740e+00
12	1.864383906383391e-01	5.592982707721965e-03	-2.681677610205356e-02	2.077994156444422e+00
13	1.871727202465446e-01	1.904874688294771e-03	-9.054089766680987e-03	2.069227845708927e+00
14	1.871726958138935e-01	-1.905123817236458e-03	9.055276522233141e-03	2.069228135898337e+00
15	1.864383190992423e-01	-5.593215900576222e-03	2.681791703803989e-02	2.077995014846544e+00
16	1.850222966598256e-01	-8.923877241148600e-03	4.351969147417154e-02	2.095157106131571e+00
17	1.830253297108597e-01	-1.168570098092992e-02	5.839066617455552e-02	2.119964639887074e+00
18	1.805872365746299e-01	-1.370524136997280e-02	7.058951921735665e-02	2.151277654869007e+00
19	1.778749338319836e-01	-1.485782460338929e-02	7.922068125312409e-02	2.187555033913622e+00
20	1.750686705918447e-01	-1.507468555995388e-02	8.339611142452681e-02	2.226855090955426e+00
21	1.723481094891506e-01	-1.434621593334140e-02	8.234812271626010e-02	2.266864968549956e+00
22	1.698798245982659e-01	-1.272147534389050e-02	7.558736845065828e-02	2.304981731716214e+00
23	1.678074930636813e-01	-1.030434110823315e-02	6.308023465585133e-02	2.338467772561094e+00
24	1.662454803856217e-01	-7.246730181935063e-03	4.539701835624928e-02	2.364690483438951e+00
25	1.652757327617737e-01	-3.739282047881972e-03	2.376845849971867e-02	2.381427710888967e+00

Copyright © 2024 by the authors. Published by the IAF, with permission and released to the IAF to publish in all forms.

Table 4. Invariant curve for out-of-plane 2D-QPO at $\iota_a \approx 5.16^\circ$, position components

k	ξ	η	ζ
1	1.754223087153171e-01	-9.928988082836664e-10	1.543484504912746e-02
2	1.754644634854834e-01	1.956180220047240e-04	1.494939179661415e-02
3	1.755804897857130e-01	3.428212637885622e-04	1.352382040240743e-02
4	1.757416629552593e-01	4.051910206936796e-04	1.124842954790033e-02
5	1.759080983641458e-01	3.673185961929460e-04	8.266951932485184e-03
6	1.760386299771464e-01	2.385969768122497e-04	4.767110224574298e-03
7	1.761009869779198e-01	5.087496327111434e-05	9.686130494815618e-04
8	1.760797576820865e-01	-1.494262141491859e-04	-2.890541932721551e-03
9	1.759801886283540e-01	-3.127795646954063e-04	-6.568656067793854e-03
10	1.758268915787892e-01	-3.987815756122341e-04	-9.835090566667423e-03
11	1.756577737296586e-01	-3.861401590033771e-04	-1.248450326711252e-02
12	1.755146752464663e-01	-2.779571799888735e-04	-1.434980504283855e-02
13	1.754330160935597e-01	-1.009847347731712e-04	-1.531299281621238e-02
14	1.754330156795099e-01	1.009828135151922e-04	-1.531299754591041e-02
15	1.755146741071178e-01	2.779557346522125e-04	-1.434981893229882e-02
16	1.756577721468477e-01	3.861395456813086e-04	-1.248452543597115e-02
17	1.758268899443968e-01	3.987819483622676e-04	-9.835119614706381e-03
18	1.759801873465069e-01	3.127808274391255e-04	-6.568690165816725e-03
19	1.760797570697278e-01	1.494280591480138e-04	-2.890578940192871e-03
20	1.761009871864225e-01	-5.087299805368397e-05	9.685754509658729e-04
21	1.760386309548832e-01	-2.385953704779329e-04	4.767074389972855e-03
22	1.759080998695914e-01	-3.673177537798750e-04	8.266920108305344e-03
23	1.757416646159808e-01	-4.051911423891372e-04	1.124840373521156e-02
24	1.755804911910079e-01	-3.428223285770261e-04	1.352380222885688e-02
25	1.754644642873755e-01	-1.956197571626862e-04	1.494938241237098e-02

Copyright © 2024 by the authors. Published by the IAF, with permission and released to the IAF to publish in all forms.

Table 5. Invariant curve for out-of-plane 2D-QPO at $\iota_a \approx 5.16^\circ$, velocity components

k	$d\xi/\tau_3$	$d\eta/\tau_3$	$d\zeta/\tau_3$
1	-1.113181744959862e-08	2.223547478984756e+00	2.717190477341536e-07
2	2.198716688171796e-03	2.222867732653639e+00	-5.533653701437727e-02
3	3.853214512912644e-03	2.220996841792658e+00	-1.071856574478356e-01
4	4.554160381947499e-03	2.218398055900158e+00	-1.522843274154531e-01
5	4.128423905336459e-03	2.215714524763969e+00	-1.878023890932389e-01
6	2.681641354997473e-03	2.213609964560102e+00	-2.115181846196791e-01
7	5.717908628802219e-04	2.212604606053235e+00	-2.219526894493306e-01
8	-1.679425699040623e-03	2.212946876352705e+00	-2.184564180793236e-01
9	-3.515415309200850e-03	2.214552205945342e+00	-2.012469026506894e-01
10	-4.482083443935343e-03	2.217023853951761e+00	-1.713961891846239e-01
11	-4.340073492515880e-03	2.219750688858643e+00	-1.307685081566547e-01
12	-3.124180777750487e-03	2.222058076077460e+00	-8.190931571056867e-02
13	-1.135056540461294e-03	2.223374821699262e+00	-2.788933111846576e-02
14	1.135034951308973e-03	2.223374828375678e+00	2.788879198085039e-02
15	3.124164527339220e-03	2.222058094449309e+00	8.190881055630729e-02
16	4.340066620000861e-03	2.219750714380090e+00	1.307680687721326e-01
17	4.482087614524364e-03	2.217023880304048e+00	1.713958431474085e-01
18	3.515429533678324e-03	2.214552226612490e+00	2.012466715973307e-01
19	1.679446398791840e-03	2.212946886225503e+00	2.184563164235277e-01
20	-5.717687336895948e-04	2.212604602691691e+00	2.219527235109946e-01
21	-2.681623352254199e-03	2.213609948796240e+00	2.115183522851181e-01
22	-4.128414386075955e-03	2.215714500491388e+00	1.878026799164202e-01
23	-4.554161806112198e-03	2.218398029122817e+00	1.522847232378153e-01
24	-3.853226423940398e-03	2.220996819133042e+00	1.071861334718482e-01
25	-2.198736255090767e-03	2.222867719723152e+00	5.533706332018902e-02